



1 **Technical note: Applicability of physics-based and machine-learning-based**  
2 **algorithms of geostationary satellite in retrieving the diurnal cycle of cloud base**  
3 **height**

4

5 Mengyuan Wang<sup>1</sup>, Min Min<sup>1\*</sup>, Jun Li<sup>2</sup>, Han Lin<sup>3</sup>, Yongen Liang<sup>1</sup>, Binlong Chen<sup>2</sup>,

6 Zhigang Yao<sup>4</sup>, Na Xu<sup>2</sup>, Miao Zhang<sup>2</sup>

7

8

9 <sup>1</sup>School of Atmospheric Sciences, Southern Marine Science and Engineering  
10 Guangdong Laboratory (Zhuhai), and Guangdong Province Key Laboratory for  
11 Climate Change and Natural Disaster Studies, Zhuhai 519082, China

12 <sup>2</sup>Key Laboratory of Radiometric Calibration and Validation for Environmental  
13 Satellites and Innovation Center for FengYun Meteorological Satellite (FYSIC),  
14 National Satellite Meteorological Center (National Center for Space Weather), China  
15 Meteorological Administration, Beijing 100081, China

16 <sup>3</sup>Key Laboratory of Spatial Data Mining and Information Sharing of Ministry of  
17 Education, National and Local Joint Engineering Research Center of Satellite  
18 Geospatial Information Technology, Fuzhou University, Fuzhou 350108, China

19 <sup>4</sup>Beijing Institute of Applied Meteorology, Beijing 100029, China

20

21

22

23 *Correspondence to:* Min Min (minm5@mail.sysu.edu.cn)

24

25

26

27

28

29

30

31

32

33



34

35 **Abstract.** Four distinct retrieval algorithms, comprising two physics-based and two  
36 machine-learning (ML) approaches, have been developed to retrieve cloud base  
37 height (CBH) and its diurnal cycle from Himawari-8 geostationary satellite  
38 observations. Validations have been conducted using the joint CloudSat/CALIOP  
39 (Cloud-Aerosol Lidar with Orthogonal Polarization) CBH products in 2017, ensuring  
40 independent assessments. Results show that the two ML-based algorithms exhibit  
41 markedly superior performance (with a correlation coefficient of  $R > 0.91$  and an  
42 absolute bias of approximately 0.8 km) compared to the two physics-based algorithms.  
43 However, validations based on CBH data from the ground-based lidar at the Lijiang  
44 station in Yunnan province and the cloud radar at the Nanjiao station in Beijing,  
45 China, explicitly present contradictory outcomes ( $R < 0.60$ ). An identifiable issue  
46 arises with significant underestimations in the retrieved CBH by both ML-based  
47 algorithms, leading to an inability to capture the diurnal cycle characteristics of CBH.  
48 The strong consistence observed between CBH derived from ML-based algorithms  
49 and the spaceborne active sensor may be attributed to utilizing the same dataset for  
50 training and validation, sourced from the CloudSat/CALIOP products. In contrast, the  
51 CBH derived from the optimal physics-based algorithm demonstrates the good  
52 agreement in diurnal variations of CBH with ground-based lidar/cloud radar  
53 observations during the daytime (with an  $R$  value of approximately 0.7). Therefore,  
54 the findings in this investigation from ground-based observations advocate for the  
55 more reliable and adaptable nature of physics-based algorithms in retrieving CBH  
56 from geostationary satellite measurements. Nevertheless, under ideal conditions, with  
57 an ample dataset of spaceborne cloud profiling radar observations encompassing the  
58 entire day for training purposes, the ML-based algorithms may hold promise in still  
59 delivering accurate CBH outputs.

60 **Key words:** Geostationary meteorological satellite; cloud base height; physics-based  
61 algorithm; machine learning.

62



## 63 **1 Introduction**

64 Clouds, comprising visible aggregates like atmospheric water droplets,  
65 supercooled water droplets, ice crystals, etc., cover roughly 70% of the Earth's surface  
66 (Stubenrauch et al., 2013). They play a pivotal role in global climate change, the  
67 hydrometeor cycle, aviation safety, and serve as a primary focus in weather  
68 forecasting and climate research, particularly storm clouds (Hansen, 2007; Hartmann  
69 and Larson, 2002). From advanced geostationary (GEO) and polar-orbiting (LEO,  
70 low earth orbit) satellite imagers, various measurable cloud properties, such as  
71 fraction, phase, top height, and optical depth, are routinely retrieved. However, the  
72 high-quality cloud geometric height (CGH) and CBH, a fundamental macro physical  
73 parameter delineating the vertical distribution of clouds, remains relatively  
74 understudied and underreported. Nonetheless, for boundary-layer clouds, the cloud  
75 base height stands as a critical parameter depending on other cloud-controlling  
76 variables. These variables encompass the cloud-base temperature (Zhu et al., 2014),  
77 cloud-base vertical velocity (Zheng et al., 2020), activation of CCN (Cloud  
78 Condensation Nuclei) at the cloud-base (Rosenfeld et al., 2016; Miller et al., 2023),  
79 and the cloud-surface decoupling state (Su et al., 2022). These factors significantly  
80 impact convective cloud development and ultimately the climate. Hence, the accurate  
81 determination of CBH and its diurnal cycle with high spatial-temporal resolution  
82 becomes very important, necessitating comprehensive investigations (Viúdez-Mora et  
83 al., 2015; Wang et al., 2020). Such efforts can provide deeper insights into potential  
84 ramifications of cloud on radiation equilibrium and global climate systems.

85 However, as one of the most crucial cloud physical parameters in atmospheric  
86 physics, the CBH poses challenges in terms of measurement or estimation from space.  
87 Presently, the primary methods for measuring CBH rely on ground-based  
88 observations, utilizing tools such as sounding balloons, Mie-scattering lidars,  
89 stereo-imaging cloud-height detection technologies, and cloud probe sensors  
90 (Forsythe et al., 2000; Hirsch et al., 2011; Seaman et al., 2017; Zhang et al., 2018;  
91 Zhou et al., 2019; Zhou et al., 2024). While *in-situ* ground-based observation methods  
92 offer highly accurate, reliable, and timely continuous CBH results, they are  
93 constrained by localized observation coverage and the sparse distribution of  
94 observation sites (Aydin and Singh, 2004). In recent decades, with the rapid



95 advancement of meteorological satellite observation technology, spaceborne  
96 observing methods have emerged that provide global cloud observations with high  
97 spatio-temporal resolution compared to conventional ground-based remote sensing  
98 methods. In this realm, satellite remote sensing techniques for measuring CBH fall  
99 primarily into two categories: active and passive methods. Advanced active remote  
100 sensing technologies like CloudSat and Cloud-Aerosol Lidar and Infrared Pathfinder  
101 Satellite Observation (CALIPSO) in the National Aeronautics and Space  
102 Administration (NASA) A-Train series can capture global cloud profiles, including  
103 CBH, with high quality by detecting unique return signals from cloud layers using  
104 onboard active millimeter wave radar or lidar. However, their viewing footprints are  
105 limited along the nadir of the orbit, implying that observation coverage remains  
106 confined primarily to a horizontal scale (Min et al., 2022; Lu et al., 2021).

107 In addition to active remote sensing methods, satellite-based passive remote  
108 sensing technologies can also play an important role in estimating CBH (Meerkötter  
109 and Bugliaro, 2009; Lu et al., 2021). As well known, the physics-based principles and  
110 retrieval methods for cloud top height (CTH) have reached maturity and are now  
111 widely employed in satellite passive remote sensing field (Heidinger and Pavolonis,  
112 2009; Wang et al., 2022). However, the corresponding physical principles or methods  
113 for measuring CBH using satellite passive imager measurements are still not entirely  
114 clear and unified (Heidinger et al., 2019; Min et al., 2020). A recent study by (Yang et  
115 al., 2021) utilized oxygen A-band data observed by the Orbiting Carbon Observatory  
116 2 (OCO-2) to retrieve single-layer marine liquid CBH. Two primary methods are  
117 prominent in retrieving CBH through passive space-based remote sensing techniques.  
118 The first method involves the extrapolation technique for retrieving CBH for clouds  
119 of the same type. For instance, (Wang et al., 2012) proposed a method to extrapolate  
120 CBH from CloudSat using spatial-temporally matched MODIS (Moderate Resolution  
121 Imaging Spectroradiometer) cloud classification data. The second physics-based  
122 retrieval method first approximates the cloud geometric thickness using its optical  
123 thickness. It then employs the previously derived CTH product to compute the  
124 correlated CBH using the respective NOAA (National Oceanic and Atmospheric  
125 Administration) SNPP/VIIRS (Suomi National Polar-orbiting Partnership/Visible  
126 Infrared Imaging Radiometer Suite) products (Noh et al., 2017). Hutchison et al. also  
127 formulated an empirical algorithm that estimates both cloud geometric thickness and  
128 CBH. This algorithm relies on statistical analyses derived from MODIS cloud optical



129 thickness and cloud liquid water path products (Hutchison et al., 2006; Hutchison,  
130 2002).

131 Machine learning (ML) has proven to be highly effective in addressing nonlinear  
132 problems within remote sensing and meteorology fields, such as precipitation  
133 estimation and CTH retrieval (Min et al., 2020; HåKansson et al., 2018; Kühnlein et  
134 al., 2014). In recent years, several previous studies have leveraged ML-based  
135 algorithms to retrieve CBH, establishing nonlinear connections between CBH and  
136 GEO satellite observations. For instance, Tan et al. (2020) integrated CTH and cloud  
137 optical properties products from Fengyun-4A (FY-4A) GEO satellite with  
138 spatial-temporally matched CBH data from CALIPSO/CloudSat (Tan et al., 2020).  
139 They developed a random forest (RF) model for CBH retrieval. Similarly, Lin et al.  
140 (2022) constructed a gradient boosted regression tree (GBRT) model using U.S.  
141 new-generation Geostationary Operational Environmental Satellites-R Series  
142 (GOES-R) Advanced Baseline Imager (ABI) level 1B radiance data and the ERA5  
143 (the fifth generation ECMWF) reanalysis dataset (Lin et al., 2022). They employed  
144 CALIPSO CBH data as labels to achieve single-layer CBH retrievals. Notably, the  
145 CBH quality of ML-based algorithms was found to surpass that of physics-based  
146 algorithms (Lin et al., 2022). Moreover, Tana et al. (2023) utilized Himawari-8 data  
147 and the random forest algorithm to develop a novel CBH algorithm, achieving a high  
148 correlation coefficient of 0.92 and a low root mean square error (RMSE) of 1.17 km  
149 (Tana et al., 2023).

150 However, these former studies did not discuss whether both physics-based and  
151 ML-based algorithms of GEO satellite could retrieve the diurnal cycle of CBH well.  
152 This gap in research could be mainly attributed to potential influences from the fixed  
153 LEO satellite (with active radar or lidar) passing time in the previous CBH retrieval  
154 model (Lin et al., 2022). As well known, there are distinct diurnal cycle  
155 characteristics of clouds in different regions across the globe (Li et al., 2022). These  
156 diurnal cycle characteristics primarily stem from the daily solar energy cycle absorbed  
157 by both the atmosphere and Earth's surface. Besides, vertical atmospheric motions are  
158 shaped by imbalances in atmospheric heating and surface configurations, also leading  
159 to a range of cloud movements and structures (Miller et al., 2018). Cloud base plays a  
160 pivotal role in weather and climate processes. It is critical for predicting fog and  
161 cloud-related visibility issues important in aviation and weather forecasting. For  
162 instance, lower cloud bases often lead to more intense rainfall. In climate modeling,



163 CBH is integral for accurate long-term weather predictions and understanding the  
164 radiative balance of the Earth, which influences global temperatures (Zheng and  
165 Rosenfeld, 2015). Hence, it is crucial to thoroughly investigate the diurnal cycle  
166 features of CBH derived from GEO satellite measurements by comparing them with  
167 ground-based radar and lidar observations (Min and Zhang, 2014; Warren and  
168 Eastman, 2014). In this study, we aim to assess the applicability and feasibility of  
169 both physics-based and ML-based algorithms of GEO satellites in capturing the  
170 diurnal cycle characteristics of CBH.

171 The subsequent sections of this paper are structured as follows. Section 2  
172 provides a concise overview of the data employed in this study. Following that,  
173 section 3 introduces the four distinct physics/ML-based CBH retrieval algorithms. In  
174 section 4, the CBH results obtained from these four algorithms are analyzed, and  
175 comparisons are drawn with spatially and temporally matched CBHs from  
176 ground-based cloud radar and lidar. Finally, section 5 encapsulates the primary  
177 conclusions and new findings derived from this study.

## 178 **2 Data**

179 In this study, observations from the Himawari-8 (H8) Advanced Himawari  
180 Imager (AHI) are utilized for the retrieval of high spatiotemporal resolution CBH.  
181 Launched successfully by the Japan Meteorological Administration on October 7,  
182 2014, the H8 geostationary satellite is positioned at 140.7°E. The AHI onboard H8  
183 encompasses 16 spectral bands ranging from 0.47  $\mu\text{m}$  to 13.3  $\mu\text{m}$ , featuring spatial  
184 resolutions of 0.5–2 km. This includes 3 visible (VIS) bands at 0.5–1 km, 3  
185 near-infrared (NIR) bands at 1–2 km, and 10 infrared (IR) bands at 2 km. The  
186 H8/AHI can scan a full disk area within 10 minutes, two specific areas within 2.5  
187 minutes, a designated area within 2.5 minutes, and two landmark areas within 0.5  
188 minutes (Iwabuchi et al., 2018). Its enhanced temporal resolution and observation  
189 frequency facilitates the tracking of rapidly changing weather systems, enabling the  
190 accurate determination of quantitative atmospheric parameters (Bessho et al., 2016).

191 Operational H8/AHI Level-1B data, accessible from July 7, 2015, are freely  
192 available on the satellite product homepage of the Japan Aerospace Exploration  
193 Agency (Letu et al., 2019). The Level-2 cloud products utilized in this study,  
194 including cloud mask (CLM), CTH, cloud effective particle radius (CER), and cloud



195 optical thickness (COT), are generated by the Fengyun satellite science product  
196 algorithm testbed (FYGAT) (Wang et al., 2019; Min et al., 2017) of the China  
197 Meteorological Administration (CMA) for various applications. It is important to note  
198 that certain crucial preliminary cloud products, such as the cloud mask, have been  
199 validated in prior studies (Wang et al., 2019; Liang et al., 2023). Nevertheless, before  
200 initiating CBH retrieval, it is imperative to validate the H8/AHI cloud optical and  
201 microphysical products from the FYGAT retrieval system. This validation is carried  
202 out by using analogous MODIS Level-2 cloud products as a reference. Additional  
203 details regarding the validation of cloud products are provided in the Appendix A  
204 section.

205 In addition to the H8/AHI Level-1/2 data, the Global Forecast System (GFS)  
206 numerical weather prediction (NWP) data are employed for CBH retrieval in this  
207 study. The variables include land/sea surface temperature and the vertical profiles of  
208 temperature, humidity, and pressure. Operated by the U.S. NOAA (Kalnay et al.,  
209 1996), the GFS serves as a global and advanced NWP system. The operational GFS  
210 system routinely delivers globally high-quality and gridded NWP data at 3-hour  
211 intervals, with four different initial forecast times per day (00:00, 06:00, 12:00, and  
212 18:00 UTC). The three-dimensional NWP data cover the Earth in a  $0.5^\circ \times 0.5^\circ$  grid  
213 interval and resolve the atmosphere with 26 vertical levels from the surface (1000 hPa)  
214 up to the top of the atmosphere (10 hPa).

215 As previously mentioned, the official MODIS Collection-6.1 Level-2 cloud  
216 product Climate Data Records are utilized in this study to validate the H8/AHI cloud  
217 products (CTH, CER, and COT) generated by the FYGAT system. MODIS sensors  
218 are onboard NASA Terra and Aqua polar-orbiting satellites. Terra functions as the  
219 morning satellite, passing through the equator from north to south at approximately  
220 10:30 local time, while Aqua serves as the afternoon satellite, traversing the equator  
221 from south to north at around 13:30 local time. As a successor to the NOAA  
222 Advanced Very High Resolution Radiometer (AVHRR), MODIS features 36  
223 independent spectral bands and a broad spectral range from  $0.4 \mu\text{m}$  (VIS) to  $14.4 \mu\text{m}$   
224 (IR), with a scanning width of 2330 km and spatial resolutions ranging from 0.25 to  
225 1.0 km. Recent studies (Baum et al., 2012; Platnick et al., 2017) have highlighted  
226 significant improvements and collective changes in cloud top, optical, and  
227 microphysical properties from Collection-5 to Collection-6.



228 In addition to the passive spaceborne imaging sensors mentioned above, the  
229 CloudSat satellite, equipped with a 94-GHz active cloud profiling radar (CPR), holds  
230 the distinction of being the first sun-synchronous orbit satellite specifically designed  
231 to observe global cloud vertical structures and properties. It is part of the A-Train  
232 (Afternoon-Train) series of satellites, akin to the Aqua satellite, launched and  
233 operated by NASA (Heymsfield et al., 2008). CALIPSO is another polar-orbiting  
234 satellite within the A-Train constellation, sharing an orbit with CloudSat and trailing  
235 it by a mere 10–15 seconds. CALIPSO is the first satellite equipped with an active  
236 dual-channel CALIOP at 532 and 1064 nm bands (Hunt et al., 2009). Both CloudSat  
237 and CALIPSO possess notable advantages over passive spaceborne sensors due to the  
238 94-GHz radar of CloudSat and the joint return signals of lidar and radar on CALIPSO.  
239 These features enhance their sensitivity to optically thin cloud layers and ensure  
240 strong penetration capability, resulting in more accurate CTH and CBH detections  
241 compared to passive spaceborne sensors (CAL\_LID\_L2\_05kmCLay-Standard-V4-10).  
242 The joint cloud type products of 2B-CLDCLASS-LIDAR, derived from both  
243 CloudSat and CALIPSO measurements, offer a comprehensive description of cloud  
244 vertical structure characteristics, cloud type, CTH, CBH, etc. The time interval  
245 between each profile in this product is approximately 3.1 seconds, and the horizontal  
246 resolution is 2.5 km (along track)×1.4 km (cross-track). Each profile is divided into  
247 125 layers with a 240-m vertical interval. For more details on  
248 2B-CLDCLASS-LIDAR products, please refer to the CloudSat official product  
249 manual (Sassen and Wang, 2008). Please note that for this study, we utilized one-year  
250 H8/AHI data and matched it with the joint CloudSat/CALIOP data from January 1 to  
251 December 31 of 2017.

### 252 **3 Physics/machine-learning based cloud-base height algorithms**

#### 253 **3.1 GEO Cloud-base height retrieval algorithm from the interface data processing** 254 **segment of the Visible Infrared Imaging Radiometer Suite**

255 The Joint Polar Satellite System (JPSS) program is a collaborative effort between  
256 NASA and NOAA. The operational CBH retrieval algorithm, part of the 30  
257 Environmental Data Records (EDR) of JPSS, can be implemented operationally  
258 through the Interface Data Processing Segment (IDPS) (Baker, 2011). In this study,  
259 our geostationary satellite CBH retrieval algorithm aligns with the IDPS CBH





260 algorithm developed by (Baker, 2011). Utilizing the geostationary H8/AHI cloud  
261 products discussed earlier, this new GEO CBH retrieval algorithm is succinctly  
262 outlined below.

263 The new GEO IDPS CBH algorithm initiates the process by first retrieving the  
264 cloud geometric thickness (CGT) from bottom to top. Subsequently, CGT is  
265 subtracted from the corresponding cloud top height (CTH) to calculate CBH (CBH =  
266 CTH – CGT). The algorithm is divided into two independent executable modules  
267 based on cloud phase, distinguishing between liquid water and ice clouds. CBH of  
268 water cloud retrieval requires Cloud Optical Thickness (COT or  $D_{COT}$ ) and Effective  
269 Radius (CER or  $R_{eff}$ ) as inputs. For ice clouds, an empirical equation is employed for  
270 CBH retrieval. However, the standard deviations of error in IDPS CBH for individual  
271 granules often exceed the JPSS VIIRS minimum uncertainty requirement of  $\pm 2$ km  
272 (Noh et al., 2017). The accuracy of IDPS algorithm-derived CBHs can be directly  
273 affected by several factors, including cloud optical thickness, cloud effective particle  
274 size, the presence of multiple-layered cloud systems, lack of solar illumination, and  
275 highly reflective surfaces such as snow or ice surfaces. For a more comprehensive  
276 understanding of this CBH algorithm, please refer to the IDPS algorithm  
277 documentation (Baker, 2011).

### 278 **3.2 GEO Cloud-base height retrieval algorithm implemented in the Clouds from** 279 **Advanced Very High Resolution Radiometer Extended system**

280 As mentioned above, the accuracy of the GEO IDPS algorithm is highly  
281 dependent on the initial input parameters such as cloud phase,  $D_{COT}$  and  $R_{eff}$ , which  
282 may introduce some uncertainties in the final retrieval results. In contrast, a more  
283 reliable statistically-based algorithm is proposed and implemented here, which is  
284 named the GEO CLAVR-x (Clouds from AVHRR Extended, NOAA's operational  
285 cloud processing system for the AVHRR) CBH algorithm, and it mainly refers to  
286 NOAA AWG CBH algorithm (ACBA). Previous studies have also demonstrated a  
287 correlation coefficient of 0.569 and a root mean square error (RMSE) of 2.3 km for  
288 the JPSS VIIRS CLAVR-x CBH algorithm. It is anticipated that this algorithm will  
289 also be employed for the NOAA GORS-R geostationary satellite imager (Noh et al.,  
290 2017; Seaman et al., 2017).

291 Similar to the GEO IDPS CBH retrieval algorithm mentioned earlier, the GEO  
292 CLAVR-x CBH retrieval algorithm also initially obtains CGT and CTH, subsequently



293 calculating CBH by subtracting CGT from CTH (CTH–CGT). However, the specific  
294 calculation method for the CGT value differs. This algorithm is suitable for both  
295 single-layer and multi-layer clouds, computing CBH using the CTH at the top layer of  
296 the cloud. In comparison with the former GEO IDPS CBH algorithm, the GEO  
297 CLAVR-x CBH algorithm considers two additional cloud types: deep convection  
298 clouds and thin cirrus clouds. For more details on this CLAVR-x CBH algorithm,  
299 please refer to the original algorithm documentation (Noh et al., 2017).

### 300 **3.3 Random-forest-based cloud-base height estimation algorithm**

301 RF, one of the most significant ML algorithms, was initially proposed and  
302 developed by (Breiman, 2001). It is widely employed to address classification and  
303 regression problems based on the law of large numbers. The law of large numbers  
304 states that when independent and identically distributed random experiments are  
305 repeatedly conducted, the average of the results will converge to the expected value as  
306 the number of trials increases. In RF algorithms, it primarily serves to increase  
307 randomness and independence in model construction, thus enhancing the model's  
308 stability and generalizability. Here, the RF method utilizes a forest of trees, serving as  
309 an integrated algorithm that enhances overall model accuracy and generalization by  
310 combining multiple weak classifiers. The final prediction is calculated through voting  
311 or averaging. The RF method is well-suited for capturing complex or nonlinear  
312 relationships between predictors and predictands. As mentioned earlier, this statistical  
313 or ML-based algorithm has been already proven successful in retrieving CTH and  
314 CBH (Min et al., 2020; Tan et al., 2020).

315 In this study, two distinct ML-based GEO CBH algorithms, namely VIS+IR and  
316 IR-single (only uses observations of H8/AHI IR channels), are devised to retrieve or  
317 predict the CBH using different sets of predictors. The RF training of the chosen  
318 predictors is formulated as follows:

$$319 \text{CBH} = RF_{\text{reg}}[x_1, x_2, \dots, x_n], \quad (1)$$

320 where  $RF_{\text{reg}}$  denotes the regression Random Forests model, and  $x_i$  represents the  $i$ th  
321 predictor. The selected predictors from H8/AHI for both the VIS+IR and IR RF  
322 model training and prediction are detailed in Table 1, mainly referencing Min et al.  
323 (2020) and Tan et al. (2020). The VIS+IR algorithm retrieves CBH based on NWP  
324 data (atmospheric temperature and altitude profiles, total precipitable water (TPW),  
325 surface temperature), surface elevation, air mass 1 (air mass 1=1/cos(view zenith



326 angle)), and air mass 2 (air mass  $2=1/\cos(\text{solar zenith angle})$ ). The rationale for  
327 choosing air mass and TPW is their ability to account for the potential absorption  
328 effect of water vapor along the satellite viewing angle. The predictors in CBH  
329 retrieval also include the IR band Brightness Temperature (BT) and VIS band  
330 reflectance. The IR-single algorithm selects the same Global Forecast System (GFS)  
331 NWP data as the VIS+IR algorithm but employs different view zenith angles and  
332 azimuth angles.

333 To optimize the RF prediction model, the hyperparameters of the RF model are  
334 tuned individually. The parameters and their dynamic ranges involved in tuning the  
335 RF prediction models include the number of trees [100, 200, 300, 400, 500], the  
336 maximum depth of trees [10, 20, 30, 40, 50], the minimum number of samples  
337 required to split an internal node [2, 4, 6, 8, 10], and the minimum number of samples  
338 required to be at a leaf node [1, 3, 5, 7, 9]. In this study, we set the smallest number of  
339 trees in the forest to 100 and the maximum depth of the tree to 40.

340 The performance of RF models will be assessed using mean absolute error  
341 (MAE), mean bias error (MBE), root mean square error (RMSE), correlation  
342 coefficient (R), and standard deviation (STD) scores based on the testing dataset.  
343 These scores mentioned above are used to understand different aspects of the  
344 predictive performance of model: MAE and RMSE provide insights into the average  
345 error magnitude, MBE indicates bias in the predictions, R evaluates the linear  
346 association between observed and predicted values, and STD assesses the variability  
347 of the predictions. In the RF IR-single algorithm, 581,783 matching points are  
348 selected from H8/AHI and CloudSat data for 2017. Seventy percent of these points  
349 are randomly assigned to the training dataset, and the remainder serves as the testing  
350 dataset. For the RF VIS+IR algorithm, a total of 418,241 matching points are chosen,  
351 with 70% randomly allocated to the training set. It's important to note that the two  
352 training datasets in CloudSat will also be used to verify the CBHs obtained by cloud  
353 radar and lidar. The statistical formulas for evaluation are as follows:

354 
$$\text{MAE} = \frac{1}{n} \sum_{i=1}^n |y_i - x_i|, \quad (2)$$

355 
$$\text{MBE} = \frac{1}{n} \sum_{i=1}^n (y_i - x_i), \quad (3)$$

356 
$$\text{RMSE} = \sqrt{\frac{1}{n} \sum_{i=1}^n (y_i - x_i)^2}, \quad (4)$$



$$357 \quad R = \frac{\sum_{i=1}^n (y_i - \bar{y})(x_i - \bar{x})}{\sqrt{\sum_{i=1}^n (y_i - \bar{y})^2} \sqrt{\sum_{i=1}^n (x_i - \bar{x})^2}}, \quad (5)$$

$$358 \quad \text{STD} = \sqrt{\frac{1}{n-1} \sum_{i=1}^n (x_i - \bar{x})^2}, \quad (6)$$

359 where  $n$  is the sample number,  $y_i$  is the  $i$ th CBH retrieval result, and  $x_i$  is the  $i$ th joint  
360 CloudSat/CALIPSO CBH product.

## 361 4 Results and Discussions

### 362 4.1 Comparisons with the joint CloudSat/CALIPSO cloud-base height product

363 The H8/AHI satellite CBH data retrieved by the four algorithms are matched  
364 spatially and temporally with the 2B-CLDCLASS-LIDAR cloud product from joint  
365 CloudSat/CALIPSO observations in 2017. Fig. 1 displays a comparison of CBH  
366 results over the full disk at 02:00 UTC on January 1, 2017, retrieved by the GEO  
367 IDPS algorithm, the GEO CLAVR-x algorithm, the RF VIS+IR algorithm, and the RF  
368 IR-single algorithm. A similar distribution pattern and magnitude of CBHs retrieved  
369 by these four independent algorithms can be observed in Fig. 1. However, notable  
370 differences exist between physics-based and ML-based algorithms. Further  
371 comparisons are conducted and analyzed with spaceborne and ground-based lidar and  
372 radar observations in the subsequent sections of this study.

373 Fig. 2 presents the density scatter plot of the CBHs retrieved from the GEO IDPS  
374 and GEO CLAVR-x algorithms compared with the CBHs from the joint  
375 CloudSat/CALIPSO product, along with the related scores of MAE, MBE, RMSE,  
376 and R calculated and labeled in each panel. The calculated R exceeds the 95%  
377 significance level ( $p < 0.05$ ). For the GEO IDPS algorithm, the R is 0.62, the MAE is  
378 1.826 km, and the MBE and RMSE are -0.232 and 2.642 km (Fig. 2a). In comparison,  
379 (Seaman et al., 2017) compared the operational VIIRS CBH product retrieved by the  
380 similar SNPP/VIIRS IDPS algorithm with the CloudSat CBH results. In their results,  
381 the R is 0.569, and the RMSE is 2.3 km. For the new GEO CLAVR-x algorithm (Fig.  
382 2b), the R is 0.647, and the RMSE is 2.91 km. The larger RMSE from two  
383 independent physics-based CBH algorithms demonstrate a slightly poorer  
384 performance and precision of these retrieval algorithms for GEO satellites.  
385 Particularly, the larger RMSEs (2.642 and 2.91 km) indicate weaker stabilities of the  
386 GEO IDPS and CLAVR-x CBH algorithms. In this figure, more samples can be found



387 near the 1:1 line, implying the good quality of retrieved CBHs. However, in stark  
388 contrast, quite a number of CBH samples retrieved by both GEO IDPS and GEO  
389 CLAVR-x algorithms (compared with the official VIIRS CBH product) fall below 1.0  
390 km, indicating relatively large errors when compared with the joint  
391 CloudSat/CALIPSO CBH product. The poor predictive performance of physics-based  
392 algorithm for samples with a CBH lower than 1 km is likely due to insufficient cloud  
393 base information in the visible band observation data. Moreover, Fig. 2 reveals that  
394 relatively large errors are also found in the CBHs lower than 2 km for the four  
395 independent algorithms, primarily caused by the weak penetration ability of VIS or IR  
396 bands on thick and low clouds.

397 Referring to the joint CloudSat/CALIPSO CBH product, Fig. 2c and 2d present  
398 the validations of the CBH results retrieved from two ML-based algorithms using the  
399 VIS+IR (only retrieving the CBH during the daytime) and IR-single models. Fig. 2c  
400 demonstrates better consistency of CBH between the VIS+IR model and the joint  
401 CloudSat/CALIPSO product with  $R = 0.905$ ,  $MAE = 0.817$  km,  $MBE = 0.425$  km,  
402 and  $RMSE = 1.706$  km. Fig. 2d also displays a relatively high  $R$  of 0.876 when  
403 validating the IR-single model, with  $MAE = 0.882$ ,  $MBE = -0.445$ , and  $RMSE =$   
404  $1.995$ . Therefore, both VIS+IR and IR-single models can obtain high-quality CBH  
405 retrieval results from geostationary imager measurements. In comparison, previous  
406 studies also proposed similar ML-based algorithms for estimating CBH using FY-4A  
407 satellite imager data. For example, (Tan et al., 2020) used the variables of CTH,  $D_{COT}$ ,  
408  $R_{eff}$ , cloud water path, longitude/latitude from FY-4A imager data to build the training  
409 and prediction model and obtained CBH with  $MAE=1.29$  km and  $R=0.80$ . In this  
410 study, except CTH, the other Level-2 products and geolocation data  
411 (longitude/latitude) used in (Tan et al., 2020) are abandoned, while the matched  
412 atmospheric profile products (such as temperature and relative humidity) from NWP  
413 data are added. These changes in ML-based model training and prediction lead to  
414 more accurate CBH retrieval results. Note that, in accordance with the previous study  
415 conducted by (Noh et al., 2017), we excluded CBH samples obtained from  
416 CloudSat/CALIPSO that were smaller than 1 km in our comparisons. This exclusion  
417 was primarily due to the presence of ground clutter contamination in the CloudSat  
418 CPR data (Noh et al., 2017).

419 Fig. 3 displays two cross-sections of CBH from various sources overlaid with  
420 CloudSat radar reflectivity (unit: dBZ) for spatially and temporally matched cases.



421 The periods covered are from 03:16 to 04:55 UTC on January 13, 2017 (154.0°E–  
422 160.0°E; 40.56°S–53.39°S) and from 05:38 to 07:17 UTC on January 14, 2017  
423 (107.1°E–107.8°E; 8.35°N–11.57°N). The CloudSat radar reflectivity and joint  
424 CloudSat/CALIPSO product provide insights into the vertical structure or distribution  
425 of clouds and their corresponding CBHs. The results from the four GEO CBH  
426 retrieval algorithms (GEO IDPS, GEO CLAVR-x, RF VIS+IR model, and RF  
427 IR-single model) mentioned earlier are individually marked with different markers in  
428 each panel. According to Fig. 3a, the GEO IDPS algorithm faces challenges in  
429 accurately retrieving CBHs for geometrically thicker cloud samples near 157°E.  
430 Optically thick mid- and upper-level cloud layers may obscure lower-level cloud  
431 layers. However, the CBH results retrieved by the GEO IDPS algorithm near 155°E  
432 (in Fig. 3a) and 107.4°E (in Fig. 3b) align with the joint CloudSat/CALIPSO CBH  
433 product. It is worth noting that the inconsistency observed between 107.2°E and  
434 107.3°E in Fig. 3b, specifically regarding the CBHs around 1 km obtained from  
435 CloudSat/CALIPSO, can likely be attributed to ground clutter contamination in the  
436 CloudSat CPR data (Noh et al., 2017). The GEO CLAVR-x algorithm achieves  
437 improved CBH results compared to the GEO IDPS algorithm. It can even retrieve  
438 CBHs for some thick cloud samples that are invalid when using the GEO IDPS  
439 algorithm. However, the CBHs from the GEO CLAVR-x algorithm are noticeably  
440 higher than those from the joint CloudSat/CALIPSO product. In contrast, the CBHs  
441 from the two ML-based algorithms show substantially better results than those from  
442 the other two physics-based algorithms. Particularly, the ML-based VIS+IR model  
443 algorithm yields the best CBH results. However, compared with those from the two  
444 physics-based algorithms, the CBHs from the two ML-based algorithms still exhibit a  
445 significant error around 5 km.

446 Since the two RF models (VIS+IR and IR-single) select 230 typical variables to  
447 fit CBHs, the important scores of these predictors in the two ML-based algorithms are  
448 ranked for better optimization. In the VIS+IR model, the top-ranked predictors are  
449 CTH and CTT from the H8/AHI Level-2 product (see Fig. B1 in Appendix B). It's  
450 important to note that  $D_{COT}$  is a crucial and sensitive factor for these ML-based  
451 algorithms. Retrieving CBH samples with relatively low  $D_{COT}$  remains challenging  
452 due to the low signal-to-noise ratio when  $D_{COT}$  is low (Lin et al., 2022). To address  
453 this issue, samples with  $D_{COT}$  less than 1.6 are filtered in the VIS+IR model, and  
454 samples with relatively large BTs at Channel-14 are filtered in the IR-single model.



455 This filtering process significantly improves the R value from 0.869 to 0.922 in the  
456 VIS+IR model and from 0.868 to 0.911 in the IR-single model. For more details on  
457 the algorithm optimization, please refer to Appendix B.

#### 458 **4.2 Comparisons with the ground-based lidar and cloud radar measurements**

459 Lidar actively emits lasers in different spectral bands into the air. When the laser  
460 signal encounters cloud particles during transmission, a highly noticeable  
461 backscattered signal is generated and received (Omar et al., 2009). When lidar  
462 measures clouds, the intensity of the echo signal from the cloud to the laser satisfies  
463 the lidar equation as follows:

$$464 \quad P(r) = C * \beta(r) * r^{-2} * \exp\left[-2 \int_0^r \sigma(z) dz\right], \quad (7)$$

465 where  $P(r)$  is the intensity of the atmospheric backscattered signal received by the  
466 laser telescope from the emission point in distance  $r$  (unit: Watt or W);  $C$  is the lidar  
467 system instrumentation constant (unit:  $\text{W}\cdot\text{km}^3\cdot\text{sr}$ );  $r$  is the detection distance (unit:  
468 km);  $\beta(r)$  is the backscattering coefficient at the emission point in distance  $r$  (unit:  
469  $\text{km}^{-1}\cdot\text{sr}^{-1}$ );  $\sigma(z)$  is the extinction coefficient at the distance emission point in distance  
470  $z$  (unit:  $\text{km}^{-1}$ ). This return signal is markedly distinct from atmospheric aerosol  
471 scattering signals and noise, making CBH easily obtainable from the signal difference  
472 or mutation (Sharma et al., 2016). In this study, continuous ground-based lidar data  
473 from the Twin Astronomy Manor in Lijiang City, Yunnan Province, China (26.454°N,  
474 100.0233°E, altitude = 3175 m) are used to evaluate the diurnal cycle characteristics  
475 of CBHs retrieved using GEO satellite algorithms (Young and Vaughan, 2009). The  
476 geographical location and photo of this station are shown in Fig. 4.

477 The ground-based lidar data at Lijiang station on December 6, 2018, and January  
478 8, 2019, are selected for validation. The number of available and spatially-temporally  
479 matched CBH sample points from ground-based lidar is 78 and 64 on December 6,  
480 2018, and January 8, 2019, respectively. Fig 5a and 5b show the point-to-point CBH  
481 comparisons between ground-based lidar and four GEO satellite CBH algorithms on  
482 December 6, 2018, and January 8, 2019. It is worth noting that the retrieved CBHs of  
483 the two physics-based algorithms on December 6, 2018, are in good agreement with  
484 the reference values from the lidar measurements, and, in particular, the GEO  
485 CLAVR-x algorithm can obtain better results. From the results on January 8, 2019,  
486 more accurate diurnal cycle characteristics of CBHs are revealed by the GEO





487 CLAVR-x algorithm than by the GEO IDPS algorithm.

488 Compared with the CBHs measured by ground-based lidar, the statistics of the  
489 results retrieved from the GEO IDPS algorithm are  $R = 0.67$ ,  $MAE = 3.093$  km,  $MBE$   
490  $= 0.856$  km, and  $RMSE = 3.609$  km (Fig. 5c). However, for cloud samples with CBH  
491 below 7.5 km, the GEO IDPS algorithm shows an obvious underestimation of CBH in  
492 Fig. 5c. For the GEO CLAVR-x algorithm, it can also be seen that the matched  
493 samples mostly lie near the 1:1 line with  $R = 0.773$  (the optimal CBH algorithm),  
494  $MAE = 1.319$  km,  $MBE = 0.222$  km, and  $RMSE = 1.598$  km. In addition, this figure  
495 also shows the CBH comparisons between the ML-based VIS+IR model/IR-single  
496 model algorithms and the lidar measurements, revealing that the retrieved CBH  
497 results from the ML-based VIS+IR model are better than those from the ML-based  
498 IR-single model algorithm. The comparison results between the CBHs of the  
499 ML-based VIS+IR model algorithm and the lidar measurements are around the 1:1  
500 line, with smaller errors and  $R = 0.599$ . In contrast, the  $R$  between the CBHs of the  
501 ML-based IR-single model algorithm and the lidar measurements is only 0.494, with a  
502 relatively large error. By comparing the retrieved CBHs with the lidar measurements  
503 at Lijiang station, it indicates that CBH results from two physics-based algorithms are  
504 remarkably more accurate, particularly that the GEO CLAVR-x algorithm can well  
505 capture diurnal variation of CBH.

506 To further assess the accuracy and quality of the diurnal cycle of CBHs retrieved  
507 with these algorithms, CBHs from another ground-based cloud radar dataset covering  
508 the entire year of 2017 are also collected and used in this study. The observational  
509 instrument is a Ka-band (35 GHz) Doppler millimeter-wave cloud radar (MMCR)  
510 located at the Beijing Nanjiao Weather Observatory (a typical urban observation site)  
511 ( $39.81^{\circ}\text{N}$ ,  $116.47^{\circ}\text{E}$ , altitude = 32 m; see Fig. 4), performing continuous and routine  
512 observations. The MMCR provides a specific vertical resolution of 30 m and a  
513 temporal resolution of 1 minute for single profile detection, based on the radar  
514 reflectivity factor. In a previous study (Zhou et al., 2019), products retrieved by this  
515 MMCR were utilized to investigate the diurnal variations of CTH and CBH, and  
516 comparisons were made between MMCR-derived CBHs and those derived from a  
517 Vaisala CL51 ceilometer. The former study also found that the average correlation  
518 coefficient ( $R$ ) of CBHs from different instruments reached up to 0.65. It is worth  
519 noting that the basic physics principle for detecting cloud base height from both  
520 spaceborne cloud profiling radar and ground-based cloud radar and lidar





521 measurements is the same. All these algorithms of detecting CBH based on the  
522 manifest change of return signals between CBH and the clear sky atmosphere in the  
523 vertical direction (Huo et al., 2019; Ceccaldi et al., 2013). The joint spaceborne  
524 CloudSat/CALIPSO detection might face limitations in penetrating extremely dense,  
525 optically thick, or areas with heavy precipitation clouds. Hence, in comparison, the  
526 CBH values gathered from ground-based lidar and cloud radar measurements are  
527 expected to be more accurate than the data derived from spaceborne  
528 CloudSat/CALIPSO detection.

529 Similar to Fig. 5, Fig. 6 presents two sample groups of CBH results from the  
530 cloud radar at Beijing Nanjiao station relative to the matched CBHs from the four  
531 retrieval algorithms (GEO IDPS, GEO CLAVR-x, ML-based IR-single, ML-based  
532 VIS+IR) on April 9–10 and July 26–28, 2017. Due to the density of points in the  
533 one-year time series, the point-to-point CBH comparison results for the entire year are  
534 not displayed here (monthly results are shown in the supplementary document).  
535 Similar to the results at Lijiang station discussed in Fig. 5, we observe better and more  
536 robust performances in retrieving diurnal cycle characteristics of CBH from the two  
537 physics-based CBH retrieval algorithms. In contrast, more underestimated CBH  
538 samples are retrieved by the two ML-based algorithms.

539 To further investigate the diurnal cycle characteristics of retrieved CBH from  
540 GEO satellite imager measurements, Fig. 7 presents box plots of the hourly CBH  
541 errors (relative to the results of cloud radar at Beijing Nanjiao station) in 2017 from  
542 the four different CBH retrieval algorithms. Remarkably, there are significant  
543 underestimations of the CBHs retrieved from the two ML-based algorithms. The  
544 ML-based VIS+IR method achieves relatively better results than the ML-based  
545 IR-single method during the daytime. Comparing the two ML-based algorithms, the  
546 errors of the IR-single model algorithm have a similar standard deviation (2.80 km) to  
547 those of the VIS+IR model algorithm (2.69 km) during the daytime. For the IR-single  
548 model algorithm, it can be applied during both daytime and nighttime, its nighttime  
549 performance degrades slightly, with an averaged RMSE (3.88 km) higher than that of  
550 daytime (3.56 km). To the best of our knowledge, there is no alternative nighttime  
551 CBH product for geostationary satellite imagers right now. The nighttime CBH of the  
552 IR-single model algorithm is the only choice that should be used with discretion.

553 Fig. 8 shows the comparisons of hourly MAE, MBE, RMSE, and R relative to the  
554 CBHs from the cloud radar at Beijing Nanjiao station during daytime between four



555 retrieval algorithms in 2017. The RMSE of the two ML-based algorithms shows  
556 stable diurnal variation. It is noted that all algorithms have lower correlation  
557 coefficients ( $R$ ) at sunrise, around 07:00 local time, which improve as the day  
558 progresses. However, the GEO CLAVR-x algorithm stands out for its relatively higher  
559 and more stable in  $R$  and RMSE during daytime.

560 Fig. 9a displays scatter plots and relevant statistics of the CBHs retrieved from  
561 the GEO IDPS algorithm against the CBHs from cloud radar. The CBHs from the  
562 GEO IDPS algorithm align well with the matched CBHs from cloud radar at Beijing  
563 Nanjiao station, with  $R = 0.515$ , MAE = 2.078 km, MBE = 1.168 km, and RMSE =  
564 2.669 km. In Fig. 9b, the GEO CLAVR-x algorithm shows better results with  $R =$   
565 0.573, MAE = 2.059 km, MBE = -0.204 km, and RMSE = 2.601 km. It is not  
566 surprising that Figs. 8c and 8d reveal obvious underestimated CBH results from the  
567 two ML-based CBH algorithms. Particularly, the CBH results from the ML-based  
568 VIS+IR model algorithm concentrate in the range of 2.5 km to 5 km. Therefore, Fig. 5  
569 to Fig. 9 further substantiates the weak diurnal variations captured by ML-based  
570 techniques, primarily attributed to the scarcity of comprehensive CBH training  
571 samples throughout the entire day. Besides, although the two robust physics-based  
572 algorithms of GEO IDPS and GEO CLAVR-x (the optimal one) can retrieve  
573 high-quality CBHs from H8/AHI data, especially the diurnal cycle of CBH during the  
574 daytime, they still struggle to retrieve CBHs below 1 km.

## 575 **5. Conclusions and discussion**

576 To explore and argue the optimal and most robust CBH retrieval algorithm from  
577 geostationary satellite imager measurements, particularly focusing on capturing the  
578 typical diurnal cycle characteristics of CBH, this study employs four different  
579 retrieval algorithms (two physics-based and two ML-based algorithms). High  
580 spatial-temporal resolution CBHs are retrieved using the H8/AHI data from 2017 and  
581 2018. To assess the accuracies of the retrieved CBHs, point-to-point validations are  
582 conducted based on spatially-temporally matched CBHs from the joint  
583 CloudSat/CALIOP product, as well as ground-based lidar and cloud radar  
584 observations in China. The main findings and conclusions are outlined below.

585 Four independent CBH retrieval algorithms, namely physics-based GEO IDPS,  
586 GEO CLAVR-x, ML-based VIS+IR, and ML-based IR-single, have been developed



587 and utilized to retrieve CBHs from GEO H8/AHI data. The two physics-based  
588 algorithms utilize cloud top and optical property products from AHI as input  
589 parameters to retrieve high spatial-temporal resolution CBHs, with operations limited  
590 to daytime. In contrast, the ML-based VIS+IR model and IR-single model algorithms  
591 use the matched joint CloudSat/CALIOP CBH product as true values for building RF  
592 prediction models. Notably, the ML-based IR-single algorithm, which relies solely on  
593 infrared band measurements, can retrieve CBH throughout the day.

594 The accuracy of CBHs retrieved from the four independent algorithms is verified  
595 using the joint CloudSat/CALIOP CBH products for the year 2017. The GEO IDPS  
596 algorithm shows an R of 0.62 and an RMSE of 2.642 km. The GEO CLAVR-x  
597 algorithm provides more accurate CBHs with an R of 0.647 and RMSE of 2.91 km.  
598 After filtering samples with optical thickness less than 1.6 and brightness temperature  
599 (at 11  $\mu\text{m}$  band) greater than 281 K, the ML-based VIS+IR and ML-based IR-single  
600 algorithms achieve higher accuracy with an R(RMSE) of 0.922(1.214 km) and  
601 0.911(1.415 km), respectively. This indicates strong agreement between the two  
602 ML-based CBH algorithms and the CloudSat/CALIOP CBH product.

603 However, in stark contrast, the results from the physics-based algorithms are  
604 superior to those from the ML-based algorithms (with R and RMSE of 0.592/2.86 km  
605 and 0.385/3.88 km, respectively) when compared with ground-based CBH  
606 observations such as lidar and cloud radar. In the comparison with the cloud radar at  
607 Beijing Nanjiao station in 2017, the R of the GEO CLAVR-x algorithm is 0.573,  
608 while the R of the GEO IDPS algorithm is 0.515. Meanwhile, notable differences are  
609 observed in the CBHs from both ML-based algorithms. Similar conclusions are also  
610 evident in the 2-day comparisons at Yunnan Lijiang station.

611 The CBH results from the two ML-based algorithms ( $R > 0.91$ ) can likely be  
612 attributed to the use of the same training and validation dataset source as the joint  
613 CloudSat/CALIOP product. However, this dataset has limited spatial coverage and  
614 small temporal variation, potentially limiting the representativeness of the training  
615 data. In contrast, the GEO CLAVR-x algorithm demonstrates the best performance  
616 and highest accuracy in retrieving CBH from geostationary satellite data. Notably, its  
617 results align well with those from ground-based lidar and cloud radar during the  
618 daytime. However, both physics-based methods, utilizing CloudSat CPR data for  
619 regression, struggle to accurately retrieve CBHs below 1 km, as the lowest 1 km  
620 above ground level of this data is affected by ground clutter.



621 Additionally, despite utilizing the same physics principles in spaceborne and  
622 ground-based lidar/radar CBH algorithms, the previous study (Thorsen et al., 2011)  
623 has highlighted differences in profiles between them. Therefore, this factor could  
624 contribute to the relatively poorer results in CBH retrieval by ML-based algorithms  
625 compared to ground-based lidar and radar. The analysis and discussion above suggest  
626 that ML-based algorithms are constrained by the size and representativeness of their  
627 datasets. Therefore, in scenarios involving a large time scope, such as climate  
628 research, it is more reasonable to opt for physics-based cloud base height algorithms.

629 Ideally, if more spaceborne cloud profiling radars with different passing times  
630 (covering all day) can be included in the training dataset, the promising ML technique  
631 will certainly generate a higher quality CBH product with more comprehensive  
632 observations. The CBH product using ML-based algorithms should continue to be  
633 improved in future work. At present, we will focus on developing physics-based  
634 algorithms for cloud base height for the next generation of geostationary  
635 meteorological satellites, to support the application of these products in weather and  
636 climate domains.

637 Besides, at night, current GEO satellite imaging instruments encounter  
638 challenges in accurately determining CBH due to limited or absent solar illumination.  
639 Because it is unable to retrieve cloud optical depth in the visible band, the current  
640 method faces limitations. However, there is potential for enhanced accuracy in  
641 deriving cloud optical and microphysical properties, as well as CBH, by incorporating  
642 the Day/Night Band (DNB) observations during nighttime in the future (Walther et al.,  
643 2013).

644

645

646 *Data availability.* The authors would like to acknowledge NASA, JMA, University of  
647 Colorado, and NOAA for freely providing the MODIS  
648 (<https://ladsweb.modaps.eosdis.nasa.gov/search>), CloudSat/CALIOP  
649 (<https://www.cloudsat.cira.colostate.edu/>), Himawari-8 (<ftp.ptree.jaxa.jp>), and GFS  
650 NWP (<ftp://nomads.ncdc.noaa.gov/GFS/Grid4>) data online, respectively.

651

652

653 *Author contributions.* MM proposed the essential research idea. MW, MM, JL, HL,



654 BC, and YL performed the analysis and drafted the manuscript. ZY and NX provided  
655 useful comments. All the authors contributed to the interpretation and discussion of  
656 results and the revision of the manuscript.

657

658

659 *Competing interests.* The authors declare that they have no conflict of interest.

660

661

662 *Acknowledgements.* The authors would like to acknowledge NASA, JMA, University  
663 of Colorado, and NOAA for freely providing satellite data online, respectively. The  
664 authors thank NOAA, NASA, and their VIIRS algorithm working groups (AWG) for  
665 freely providing the VIIRS cloud base height algorithm theoretical basic  
666 documentations (ATBD). In addition, the authors appreciate the power computer tools  
667 developed by the Python and scikit-learn groups (<http://scikit-learn.org>). Besides the  
668 authors also thank Rundong Zhou and Pan Xia for drawing some pictures of this  
669 manuscript. Last but not the least, the authors sincerely thank Prof. Yong Zhang and  
670 Prof. Jianping Guo for freely providing cloud base height results retrieved by  
671 ground-based cloud radar at Beijing Nanjiao station. This work was supported partly  
672 by the Natural Science Foundation of Shanghai (No. 21ZR1419800), the Guangdong  
673 Major Project of Basic and Applied Basic Research (Grant 2020B0301030004),  
674 National Natural Science Foundation of China under Grants 42175086 and U2142201,  
675 FengYun Meteorological Satellite Innovation Foundation under Grant  
676 FY-APP-ZX-2022.0207, Innovation Group Project of Southern Marine Science and  
677 Engineering Guangdong Laboratory (Zhuhai) (No. 311022006), and the Science and  
678 Technology Planning Project of Guangdong Province (2023B1212060019). We  
679 would like to thank the editor and anonymous reviewers for their thoughtful  
680 suggestions and comments.

681

682



## 683 Appendix A

684 Based on the previously discussed description of two physics-based cloud base  
685 height (CBH) retrieval algorithms (GEO IDPS and GEO CLAVR-x retrieval  
686 algorithms), cloud products such as cloud top height (CTH), effective particle radius  
687 ( $R_{\text{eff}}$ ), and cloud optical thickness ( $D_{\text{COT}}$ ) will be utilized in both algorithms. To  
688 validate the reliability of these cloud products derived from the Advanced Himawari  
689 Imager (AHI) aboard the Himawari-8 (H8), a pixel-by-pixel comparison is conducted  
690 with analogous MODIS Collection-6.1 Level-2 cloud products. Both Aqua and Terra  
691 MODIS Level-2 cloud products (MOD06 and MYD06) are accessible for free  
692 download from the MODIS official website. For verification purposes, the  
693 corresponding Level-2 cloud products from January, April, July, and October of 2018  
694 are chosen to assess CTH,  $D_{\text{COT}}$ , and  $R_{\text{eff}}$  retrieved by H8/AHI.

695 Fig. S2 (in the supplementary document) shows the spatially-temporally matched  
696 case comparisons of CTH,  $D_{\text{COT}}$  and  $R_{\text{eff}}$  from H8/AHI and Terra/MODIS (MYD06)  
697 at 03:30 UTC on January 15, 2018. It can be seen that the CTH,  $D_{\text{COT}}$  and  $R_{\text{eff}}$  from  
698 H8/AHI are in good agreement with the matched MODIS cloud products. However,  
699 there are still some differences in  $R_{\text{eff}}$  at the regions near 35°N, 110°E in Figs. S2d  
700 and S2c. The underestimated  $R_{\text{eff}}$  values from H8/AHI relative to MODIS have been  
701 reported in previous studies. (Letu et al., 2019) compared the ice cloud products  
702 retrieved from AHI and MODIS, and concluded that the  $R_{\text{eff}}$  from both products differ  
703 remarkably in the ice cloud region and the  $D_{\text{COT}}$  from them are roughly similar.  
704 However, the  $D_{\text{COT}}$  from AHI data is higher in some areas. Looking again at the cloud  
705 optical thickness that at the same time, the slight underestimation of H8/AHI  $D_{\text{COT}}$   
706 can be found in Figs. S2e and S2f. Fig. S3 (in the supplementary document) shows  
707 another case at 02:10 UTC on January 15, 2018. Despite of the good consistence  
708 between H8/AHI and MODIS cloud products, there are slight differences in CTH in  
709 the area around 40°S–40.5°S, 100°E–110°E in Figs. S3a and S3b. Besides, as shown  
710 in Fig. S2, there are still underestimations in the  $R_{\text{eff}}$  of H8/AHI.

711 To further compare and validate these three H8/AHI cloud products, the  
712 spatially-temporally matched samples from H8/AHI and Aqua/Terra MODIS in four  
713 months of 2018 are counted within the three intervals of 0.1 km (CTH), 1.0  $\mu\text{m}$  ( $R_{\text{eff}}$ ),  
714 and 1 ( $D_{\text{COT}}$ ) in Fig. S4 (in the supplementary document). The corresponding mean  
715 absolute error, mean bias error, root mean square error and correlation coefficient ( $R$ )  
716 values are also calculated and marked in each subfigure. As can be seen, the  $R$  of



717 CTH is around 0.75 in all four months and is close to 0.8 in August. The results of  
718  $D_{\text{COT}}$  show the highest  $R$ , reaching above 0.8. In contrast, the underestimation trend in  
719  $R_{\text{eff}}$  is also shown in this figure. These different consistencies between two  
720 satellite-retrieved cloud products may be attributed to: (1) different spatial-temporal  
721 resolutions between H8/AHI and MODIS; (2) different wavelength bands, bulk  
722 scattering model, and specific algorithm used for retrieving cloud products; (3)  
723 different view zenith angle between GEO and low-earth-orbit satellite platforms (Letu  
724 et al., 2019). In addition, other external factors such as surface type also can affect the  
725 retrieval of cloud product. However, according to Fig. S4, the bulk of the analyzed  
726 samples are still around the 1:1 line, indicating the good quality of H8/AHI cloud  
727 products.

728

## 729 **Appendix B**

730 The ML-based visible (VIS)+infrared (IR) model algorithm mentioned above  
731 uses 230 typical variables (see Table 1) as model predictors, and the importance  
732 scores of top-30 predictors are ranked in Fig. S5 (in the supplementary document). It  
733 can be seen that the most important variables are CTH and cloud top temperature, and  
734  $D_{\text{COT}}$  is an important or sensitive factor affecting these two quantities. A sensitivity  
735 test is also performed to further investigate the potential influence of  $D_{\text{COT}}$  on the  
736 CBH retrieval by the VIS+IR model (see Table S1 in the supplementary document).  
737 From Fig. S7a, we find that the samples with  $D_{\text{COT}}$  lower than 5 cause the relatively  
738 large CBH errors compared with the matched CBHs from the joint CALIPSO  
739 (Cloud-Aerosol Lidar and Infrared Pathfinder Satellite Observation)/CloudSat  
740 product.

741 According to the results in this Fig. S7b, we may filter the samples with  
742 relatively small  $D_{\text{COT}}$  to further improve the accuracy of CBH retrieval by the VIS+IR  
743 model (see Table S1). Fig. B3b shows that after filtering the samples with the  $D_{\text{COT}}$   
744 less than 1.6, the  $R$  increases from 0.895 to 0.922, implying a better performance of  
745 CBH retrieval. According to the ranking of predictor importance (see Fig. S6 in the  
746 supplementary document), we also conduct another sensitivity test on the BT  
747 observed by H8/AHI IR Channel-14 (Cha14) at 11  $\mu\text{m}$ , which plays an important role  
748 in the IR-single model. Fig. S7c shows that the BT values of H8/AHI Channel-14  
749 ranges from 160 K to 316 K, and the samples with BT higher than 300 K show large  
750 CBH errors. Similarly, by filtering the samples with BT higher than 281 K, we can get



751 a better IR-single model algorithm for retrieving high-quality CBH (see Table S2 in  
752 the supplementary document). Fig. S7d also proves that the  $R$  value increases from  
753 0.868 to 0.911.  
754

## 755 Reference

- 756 Aydin, K. and Singh, J.: Cloud Ice Crystal Classification Using a 95-GHz Polarimetric Radar, *Journal of*  
757 *Atmospheric and Oceanic Technology*, 21, 1679–1688, <https://doi.org/10.1175/JTECH1671.1>,  
758 2004.
- 759 Baker, N.: Joint Polar Satellite System (JPSS) VIIRS Cloud Base Height Algorithm Theoretical Basis  
760 Document (ATBD), 2011.
- 761 Baum, B., Menzel, W. P., Frey, R., Tobin, D., Holz, R., and Ackerman, S.: MODIS cloud top property  
762 refinements for Collection 6, *Journal of Applied Meteorology and Climatology*, 51, 1145-1163,  
763 10.1175/JAMC-D-11-0203.1, 2012.
- 764 Bessho, K., Date, K., Hayashi, M., Ikeda, A., Imai, T., Inoue, H., Kumagai, Y., Miyakawa, T., Murata, H.,  
765 Ohno, T., Okuyama, A., Oyama, R., Sasaki, Y., Shimazu, Y., Shimoji, K., Sumida, Y., Suzuki, M.,  
766 Taniguchi, H., Tsuchiyama, H., Uesawa, D., Yokota, H., and Yoshida, R.: An introduction to  
767 Himawari-8/9—Japan's new-generation geostationary meteorological satellites, *Journal of*  
768 *the Meteorological Society of Japan*, 94, 151-183, 10.2151/jmsj.2016-009, 2016.
- 769 Breiman, L.: Random forests, *Machine Learning*, 45, 5-32, 2001.
- 770 Ceccaldi, M., Delanoë, J., Hogan, R. J., Pounder, N. L., Protat, A., and Pelon, J.: From CloudSat-CALIPSO  
771 to EarthCare: Evolution of the DARDAR cloud classification and its comparison to airborne  
772 radar-lidar observations, *Journal of Geophysical Research: Atmospheres*, 118, 7962-7981,  
773 10.1002/jgrd.50579, 2013.
- 774 Forsythe, J. M., Haar, T. H. V., and Reinke, D. L.: Cloud-Base height estimates using a combination of  
775 Meteorological Satellite Imagery and Surface Reports, *Journal of Applied Meteorology and*  
776 *Climatology*, 39, 2336–2347,  
777 [https://doi.org/10.1175/1520-0450\(2000\)039<2336:CBHEUA>2.0.CO;2](https://doi.org/10.1175/1520-0450(2000)039<2336:CBHEUA>2.0.CO;2), 2000.
- 778 Håkansson, N., Adok, C., Thoss, A., Scheirer, R., and Hörnquist, S.: Neural network cloud top pressure  
779 and height for MODIS, *Atmospheric Measurement Techniques*, 11, 3177–3196,  
780 10.5194/amt-11-3177-2018, 2018.
- 781 Hansen, B.: A Fuzzy Logic–Based Analog Forecasting System for Ceiling and Visibility, *Weather and*  
782 *Forecasting*, 22, 1319-1330, 10.1175/2007waf2006017.1, 2007.
- 783 Hartmann, D. L. and Larson, K.: An important constraint on tropical cloud - climate feedback, *Geophys*  
784 *Res Lett*, 29, 12-11-12-14, 10.1029/2002gl015835, 2002.
- 785 Heidinger, A. and Pavolonis, M.: Gazing at cirrus clouds for 25 years through a split window, part 1:  
786 Methodology, *Journal of Applied Meteorology and Climatology*, 48, 1110-1116,  
787 10.1175/2008JAMC1882.1, 2009.
- 788 Heidinger, A. K., Bearson, N., Foster, M. J., Li, Y., Wanzong, S., Ackerman, S., Holz, R. E., Platnick, S., and  
789 Meyer, K.: Using sounder data to improve cirrus cloud height estimation from satellite  
790 imagers, *Journal of Atmospheric and Oceanic Technology*, 36, 1331-1342,  
791 10.1175/jtech-d-18-0079.1, 2019.





- 792 Heymsfield, A. J., Bansemer, A., Matrosov, S., and Tian, L.: The 94-GHz radar dim band: Relevance to  
793 ice cloud properties and CloudSat, *Geophys. Res. Lett.*, 35, 10.1029/2007GL031361, 2008.
- 794 Hirsch, E., Agassi, E., and Koren, I.: A novel technique for extracting clouds base height using ground  
795 based imaging, *Atmospheric Measurement Techniques*, 4, 117-130, 10.5194/amt-4-117-2011,  
796 2011.
- 797 Hunt, W. H., Winker, D. M., Vaughan, M. A., Powell, K. A., Lucker, P. L., and Weimer, C.: CALIPSO lidar  
798 description and performance assessment, *J. Atmos. Oceanic. Technol.*, 26, 2009.
- 799 Huo, J., Bi, Y., Lü, D., and Duan, S.: Cloud Classification and Distribution of Cloud Types in Beijing Using  
800 Ka-Band Radar Data, *Advances in Atmospheric Sciences*, 36, 793-803,  
801 10.1007/s00376-019-8272-1, 2019.
- 802 Hutchison, K., Wong, E., and Ou, S. C.: Cloud base heights retrieved during night-time conditions with  
803 MODIS data, *Int J Remote Sens*, 27, 2847-2862, 10.1080/01431160500296800, 2006.
- 804 Hutchison, K. D.: The retrieval of cloud base heights from MODIS and three-dimensional cloud fields  
805 from NASA's EOS Aqua mission, *Int J Remote Sens*, 23, 5249-5265,  
806 10.1080/01431160110117391, 2002.
- 807 Iwabuchi, H., Putri, N. S., Saito, M., Tokoro, Y., Sekiguchi, M., Yang, P., and Baum, B. A.: Cloud Property  
808 Retrieval from Multiband Infrared Measurements by Himawari-8, *Journal of the  
809 Meteorological Society of Japan. Ser. II*, 96B, 27-42, 10.2151/jmsj.2018-001, 2018.
- 810 Kalnay, E., Kanamitsu, M., Kistler, R., Collins, W., Deaven, D., Gandin, L., Iredell, M., Saha, S., White, G.,  
811 Woollen, J., Zhu, Y., Leetmaa, A., Reynolds, R., Chelliah, M., Ebisuzaki, W., W.Higgins, Janowiak,  
812 J., Mo, K. C., Ropelewski, C., and Wang, J.: The NCEP NCAR 40-Year Reanalysis Project, 1996.
- 813 Kühnlein, M., Appelhans, T., Thies, B., and Nauß, T.: Precipitation Estimates from MSG SEVIRI Daytime,  
814 Nighttime, and Twilight Data with Random Forests, *Journal of Applied Meteorology and  
815 Climatology*, 53, 2457-2480, 10.1175/jamc-d-14-0082.1, 2014.
- 816 Letu, H., Nagao, T. M., Nakajima, T. Y., Riedi, J., Ishimoto, H., Baran, A. J., Shang, H., Sekiguchi, M., and  
817 Kikuchi, M.: Ice cloud properties from Himawari-8/AHI next-generation geostationary satellite:  
818 Capability of the AHI to monitor the DC cloud generation process, *IEEE Transactions on  
819 Geoscience and Remote Sensing*, 57, 3229-3239, 10.1109/tgrs.2018.2882803, 2019.
- 820 Li, Y., Yi, B., and Min, M.: Diurnal variations of cloud optical properties during day-time over China  
821 based on Himawari-8 satellite retrievals, *Atmospheric Environment*, 277, 119065,  
822 10.1016/j.atmosenv.2022.119065, 2022.
- 823 Liang, Y., Min, M., Yu, Y., Wang, X., and Xia, P.: Assessing diurnal cycle of cloud covers of Fengyun-4A  
824 geostationary satellite based on the manual observation data in China, *IEEE Transactions on  
825 Geoscience and Remote Sensing*, 61, 10.1109/TGRS.2023.3256365, 2023.
- 826 Lin, H., Li, Z., Li, J., Zhang, F., Min, M., and Menzel, W. P.: Estimate of daytime single-layer cloud base  
827 height from Advanced Baseline Imager measurements, *Remote Sensing of Environment*, 274,  
828 112970, 10.1016/j.rse.2022.112970, 2022.
- 829 Lu, X., Mao, F., Rosenfeld, D., Zhu, Y., Pan, Z., and Gong, W.: Satellite retrieval of cloud base height and  
830 geometric thickness of low-level cloud based on CALIPSO, *Atmospheric Chemistry and  
831 Physics*, 21, 10.5194/acp-21-11979-2021, 2021.
- 832 Meerkötter, R. and Bugliaro, L.: Diurnal evolution of cloud base heights in convective cloud fields from  
833 MSG/SEVIRI data *Atmospheric Chemistry and Physics*, 9, 1767-1778,  
834 10.5194/acp-9-1767-2009, 2009.
- 835 Miller, R. M., Rauber, R. M., Girolamo, L. D., Rilloraza, M., Fu, D., McFarquhar, G. M., Nesbitt, S. W.,



- 836 Ziemba, L. D., Woods, S., and Thornhill, K. L.: Influence of natural and anthropogenic aerosols  
837 on cloud base droplet size distributions in clouds over the South China Sea and West Pacific,  
838 *Atmospheric Chemistry and Physics*, 23, 8959–8977, 10.5194/acp-23-8959-2023, 2023.
- 839 Miller, S. D., Rogers, M. A., Haynes, J. M., Sengupta, M., and Heidinger, A. K.: Short-term solar  
840 irradiance forecasting via satellite/model coupling, *Solar Energy*, 168, 102–117,  
841 10.1016/j.solener.2017.11.049, 2018.
- 842 Min, M. and Zhang, Z.: On the influence of cloud fraction diurnal cycle and sub-grid cloud optical  
843 thickness variability on all-sky direct aerosol radiative forcing, *Journal of Quantitative  
844 Spectroscopy and Radiative Transfer*, 142, 25–36, 10.1016/j.jqsrt.2014.03.014., 2014.
- 845 Min, M., Li, J., Wang, F., Liu, Z., and Menzel, W. P.: Retrieval of cloud top properties from advanced  
846 geostationary satellite imager measurements based on machine learning algorithms, *Remote  
847 Sensing of Environment*, 239, 111616, 10.1016/j.rse.2019.111616 2020.
- 848 Min, M., Chen, B., Xu, N., He, X., Wei, X., and Wang, M.: Nonnegligible diurnal and long-term variation  
849 characteristics of the calibration biases in Fengyun-4A/AGRI infrared channels based on the  
850 oceanic drifter data, *IEEE Transactions on Geoscience and Remote Sensing*, 60, 1–15,  
851 10.1109/TGRS.2022.3160450, 2022.
- 852 Min, M., Wu, C., Li, C., Liu, H., Xu, N., Wu, X., Chen, L., Wang, F., Sun, F., Qin, D., Wang, X., Li, B., Zheng,  
853 Z., Cao, G., and Dong, L.: Developing the science product algorithm testbed for Chinese  
854 next-generation geostationary meteorological satellites: FengYun-4 series, *Journal of  
855 Meteorological Research*, 31, 708–719, 10.1007/s13351-017-6161-z, 2017.
- 856 Noh, Y.-J., Forsythe, J. M., Miller, S. D., Seaman, C. J., Li, Y., Heidinger, A. K., Lindsey, D. T., Rogers, M. A.,  
857 and Partain, P. T.: Cloud-base height estimation from VIIRS. Part II: A statistical algorithm  
858 based on A-Train satellite data, *Journal of Atmospheric and Oceanic Technology*, 34, 585–598,  
859 10.1175/JTECH-D-16-0110.1, 2017.
- 860 Omar, A., Winker, D., Kittaka, C., Vaughan, M., Liu, Z., Hu, Y., Treppe, C., Rogers, R., Ferrare, R., Kuehn,  
861 R., and Hostetler, C.: The CALIPSO automated aerosol classification and lidar ratio selection  
862 algorithm, *J. Atmos. Oceanic. Technol.*, 26, 1994–2014, 10.1175/2009JTECHA1231, 2009.
- 863 Platnick, S., Meyer, K. G., King, M. D., Wind, G., Amarasinghe, N., Marchant, B., Arnold, G. T., Zhang, Z.,  
864 Hubanks, P. A., Holz, R. E., Yang, P., Ridgway, W. L., and Riedi, J.: The MODIS cloud optical and  
865 microphysical products: Collection 6 updates and examples from Terra and Aqua, *IEEE Trans  
866 Geosci Remote Sens*, 55, 502–525, 10.1109/TGRS.2016.2610522, 2017.
- 867 Rosenfeld, D., Zheng, Y., Hashimshoni, E., Pohlker, M. L., Jefferson, A., Pohlker, C., Yu, X., Zhu, Y., Liu, G.,  
868 Yue, Z., Fischman, B., Li, Z., Giguzin, D., Goren, T., Artaxo, P., Barbosa, H. M., Poschl, U., and  
869 Andreae, M. O.: Satellite retrieval of cloud condensation nuclei concentrations by using  
870 clouds as CCN chambers, *Proc. Natl. Acad. Sci.*, 113, 5828–5834, 10.1073/pnas.1514044113,  
871 2016.
- 872 Sassen, K. and Wang, Z.: Classifying clouds around the globe with the CloudSat radar: 1-year of results,  
873 *Geophys. Res. Lett.*, 35, 1–5, doi:10.1029/2007GL032591, 2008.
- 874 Seaman, C. J., Noh, Y.-J., Miller, S. D., Heidinger, A. K., and Lindsey, D. T.: Cloud-base height estimation  
875 from VIIRS. Part I: Operational algorithm validation against CloudSat, *Journal of Atmospheric  
876 and Oceanic Technology*, 34, 567–583, 10.1175/jtech-d-16-0109.1, 2017.
- 877 Sharma, S., Vaishnav, R., Shukla, M. V., Kumar, P., Kumar, P., Thapliyal, P. K., Lal, S., and Acharya, Y. B.:  
878 Evaluation of cloud base height measurements from Ceilometer CL31 and MODIS satellite  
879 over Ahmedabad, India, *Atmospheric Measurement Techniques*, 9, 711–719,



- 880 10.5194/amt-9-711-2016, 2016.
- 881 Stubenrauch, C. J., Rossow, W. B., Kinne, S., Ackerman, S., Cesana, G., Chepfer, H., Di Girolamo, L.,  
882 Getzewich, B., Guignard, A., Heidinger, A., Maddux, B. C., Menzel, W. P., Minnis, P., Pearl, C.,  
883 Platnick, S., Poulsen, C., Riedi, J., Sun-Mack, S., Walther, A., Winker, D., Zeng, S., and Zhao, G.:  
884 Assessment of global cloud datasets from satellites: project and database initiated by the  
885 GEWEX radiation panel, *Bulletin of the American Meteorological Society*, 94, 1031-1049,  
886 10.1175/bams-d-12-00117.1, 2013.
- 887 Su, T., Zheng, Y., and Li, Z.: Methodology to determine the coupling of continental clouds with surface  
888 and boundary layer height under cloudy conditions from lidar and meteorological data,  
889 *Atmospheric Chemistry and Physics*, 22, 1453-1466, 10.5194/acp-22-1453-2022, 2022.
- 890 Tan, Z., Huo, J., Ma, S., Han, D., Wang, X., Hu, S., and Yan, W.: Estimating cloud base height from  
891 Himawari-8 based on a random forest algorithm, *Int J Remote Sens*, 42, 2485-2501,  
892 10.1080/01431161.2020.1854891, 2020.
- 893 Tana, G., Ri, X., Shi, C., Ma, R., Letu, H., Xu, J., and Shi, J.: Retrieval of cloud microphysical properties  
894 from Himawari-8/AHI infrared channels and its application in surface shortwave downward  
895 radiation estimation in the sun glint region, *Remote Sensing of Environment*, 29, 113548,  
896 10.1016/j.rse.2023.113548, 2023.
- 897 Thorsen, T. J., Fu, Q., and Comstock, J.: Comparison of the CALIPSO satellite and ground-based  
898 observations of cirrus clouds at the ARM TWP sites, *Journal of Geophysical Research:  
899 Atmospheres*, 116, 10.1029/2011jd015970, 2011.
- 900 Viúdez-Mora, A., Costa-Surós, M., Calbó, J., and González, J. A.: Modeling atmospheric longwave  
901 radiation at the surface during overcast skies: The role of cloud base height, *Journal of  
902 Geophysical Research: Atmospheres*, 120, 199-214, 10.1002/2014jd022310, 2015.
- 903 Wang, F., Min, M., Xu, N., Liu, C., Wang, Z., and Zhu, L.: Effects of linear calibration errors at low  
904 temperature end of thermal infrared band: Lesson from failures in cloud top property  
905 retrieval of FengYun-4A geostationary satellite, *IEEE Transactions on Geoscience and Remote  
906 Sensing*, 60, 5001511, 10.1109/TGRS.2022.3140348, 2022.
- 907 Wang, T., Shi, J., Ma, Y., Letu, H., and Li, X.: All-sky longwave downward radiation from satellite  
908 measurements: General parameterizations based on LST, column water vapor and cloud top  
909 temperature, *ISPRS Journal of Photogrammetry and Remote Sensing*, 161, 52-60,  
910 10.1016/j.isprsjprs.2020.01.011, 2020.
- 911 Wang, X., Min, M., Wang, F., Guo, J., Li, B., and Tang, S.: Intercomparisons of cloud mask product  
912 among Fengyun-4A, Himawari-8 and MODIS, *IEEE Transactions on Geoscience and Remote  
913 Sensing*, 57, 8827-8839, 10.1109/TGRS.2019.2923247 2019.
- 914 Wang, Z., Vane, D., Stephens, G., Reinke, D., and TBD: Level 2 combined radar and lidar cloud scenario  
915 classification product process description and interface control document, 2012.
- 916 Warren, S. G. and Eastman, R.: Diurnal Cycles of Cumulus, Cumulonimbus, Stratus, Stratocumulus, and  
917 Fog from Surface Observations over Land and Ocean, *J Climate*, 27, 2386-2404,  
918 10.1175/jcli-d-13-00352.1, 2014.
- 919 Yang, J., Li, S., Gong, W., Min, Q., Mao, F., and Pan, Z.: A fast cloud geometrical thickness retrieval  
920 algorithm for single-layer marine liquid clouds using OCO-2 oxygen A-band measurements,  
921 *Remote Sensing of Environment*, 256, 10.1016/j.rse.2021.112305, 2021.
- 922 Young, S. A. and Vaughan, M. A.: The retrieval of profiles of particulate extinction from Cloud Aerosol  
923 Lidar Infrared Pathfinder Satellite Observations (CALIPSO) data: Algorithm description, J.



924 Atmos. Oceanic. Technol., 26, 1105-1119, 10.1175/2008JTECHA1221.1, 2009.

925 Zhang, Y., Zhang, L., Guo, J., Feng, J., Cao, L., Wang, Y., Zhou, Q., Li, L., Li, B., Xu, H., Liu, L., An, N., and  
926 Liu, H.: Climatology of cloud-base height from long-term radiosonde measurements in China,  
927 Advances in Atmospheric Sciences, 35, 158-168, 10.1007/s00376-017-7096-0, 2018.

928 Zheng, Y. and Rosenfeld, D.: Linear relation between convective cloud base height and updrafts and  
929 application to satellite retrievals, Geophys Res Lett, 42, 6485-6491, 10.1002/2015gl064809,  
930 2015.

931 Zheng, Y., Sakradzija, M., Lee, S.-S., and Li, Z.: Theoretical Understanding of the Linear Relationship  
932 between Convective Updrafts and Cloud-Base Height for Shallow Cumulus Clouds. Part II:  
933 Continental Conditions, J Atmos Sci, 77, 1313-1328, 10.1175/jas-d-19-0301.1, 2020.

934 Zhou, Q., Zhang, Y., Li, B., Li, L., Feng, J., Jia, S., Lv, S., Tao, F., and Guo, J.: Cloud-base and cloud-top  
935 heights determined from a ground-based cloud radar in Beijing, China, Atmospheric  
936 Environment, 201, 381-390, 10.1016/j.atmosenv.2019.01.012, 2019.

937 Zhou, R., Pan, X., Xiaohu, Z., Na, X., and Min, M.: Research progress and prospects of atmospheric  
938 motion vector based on meteorological satelliteimages, Reviews of Geophysics and Planetary  
939 Physics (In Chinese), 55, 184-194, 10.19975/j.dqyxx.2022-077, 2024.

940 Zhu, Y., Rosenfeld, D., Yu, X., Liu, G., Dai, J., and Xu, X.: Satellite retrieval of convective cloud base  
941 temperature based on the NPP/VIIRS Imager, Geophys Res Lett, 41, 1308-1313,  
942 10.1002/2013gl058970, 2014.

943

944

945

946

947

948

949

950

951

952

953

954

955

956

957

958

959

960



961

962

963

**Tables and Figures**

964

965 **Table 1.** Predictand and predictor variables for both visible (VIS)+infrared (IR) model

966 and IR-single regression model training, which are divided according to the different

967 predictor variables from satellite and NWP data

Predictand	Cloud base height from the joint CloudSat/CALIPSO product	
Predictor [satellite measurements]	IR-single	BT(3.9µm), BT(6.2µm), BT(6.9µm), BT(7.3µm), BT(8.6µm), BT(9.6µm), BT(10.4µm), BT(11.2µm), BT(12.4µm), BT(13.3µm), BTD(11.2–12.4µm), BTD(11.2–13.3µm) [Unit = K], Air Mass (1/cos(VZA)), View azimuth angles [Unit = degree], Cloud top height from H8/AHI [unit: m], Cloud top temperature from H8/AHI [unit: K]
	VIS+IR	Ref(0.47µm), Ref(0.51µm), Ref(0.64µm), Ref(0.86µm), Ref(1.64µm), Ref(2.25µm), BT(3.9µm), BT(6.2µm), BT(6.9µm), BT(7.3µm), BT(8.6µm), BT(9.6µm), BT(10.4µm), BT(11.2µm), BT(12.4µm), BT(13.3µm), BTD(11.2–12.4µm), BTD(11.2–13.3µm) [Unit = K], Air Mass(1/cos(VZA)), Air Mass(1/cos(SZA)), View/Solar Azimuth angles [Unit = degree], Cloud top height from H8/AHI [unit: m], Cloud top temperature from H8/AHI [unit: K]
Predictor [GFS NWP]	IR-single/	Altitude profile (from surface to about 21 km, 67 layers) [unit: m], Temperature profile (from surface to about 21 km, 67 layers) [unit: K], Relative humidity profile (from surface to about 21 km, 67 layers) [unit: %], Total precipitable water, Surface temperature [unit: K]
	VIS+IR	
Predictor [other]	IR-single/ VIS+IR	Surface elevation [unit: m]

968 Notes: VZA = view zenith angle [unit: degree]; SZA = solar zenith angle [unit:

969 degree]

970

971

972

973

974

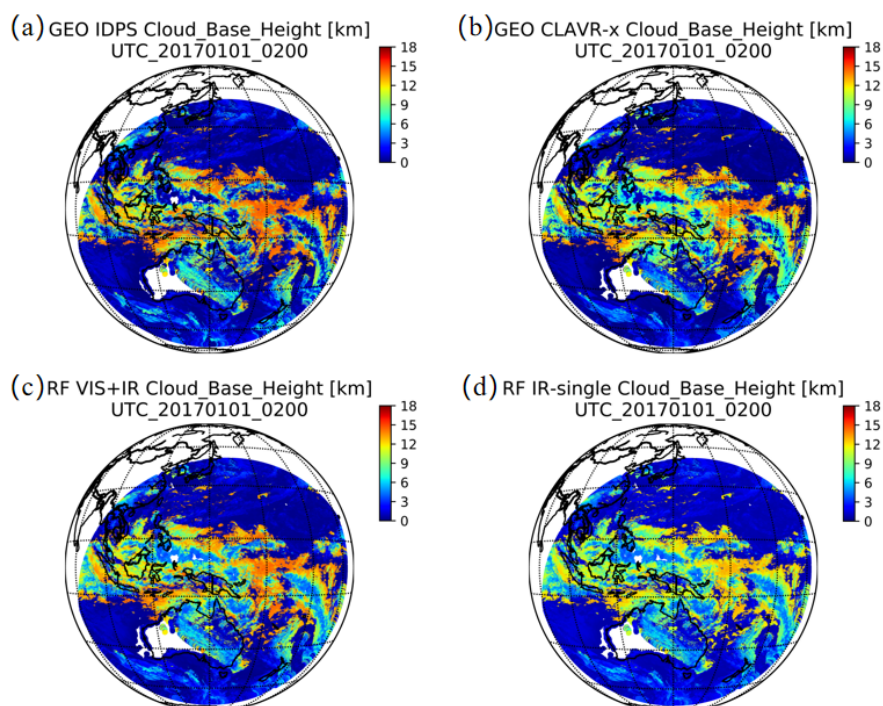
975

976

977



978  
979  
980  
981  
982



983

984 **Figure 1.** Comparison of full disk CBH results retrieved by the four-independent  
985 algorithms at 02:00 UTC on January 1, 2017. (a) GEO IDPS algorithm, (b) GEO  
986 Clouds from AVHRR Extended (CLAVR-x) algorithm, (c) ML-based (RF, random  
987 forest) VIS+IR algorithm and (d) ML-based (RF) IR-single algorithm.

988

989

990

991

992

993

994

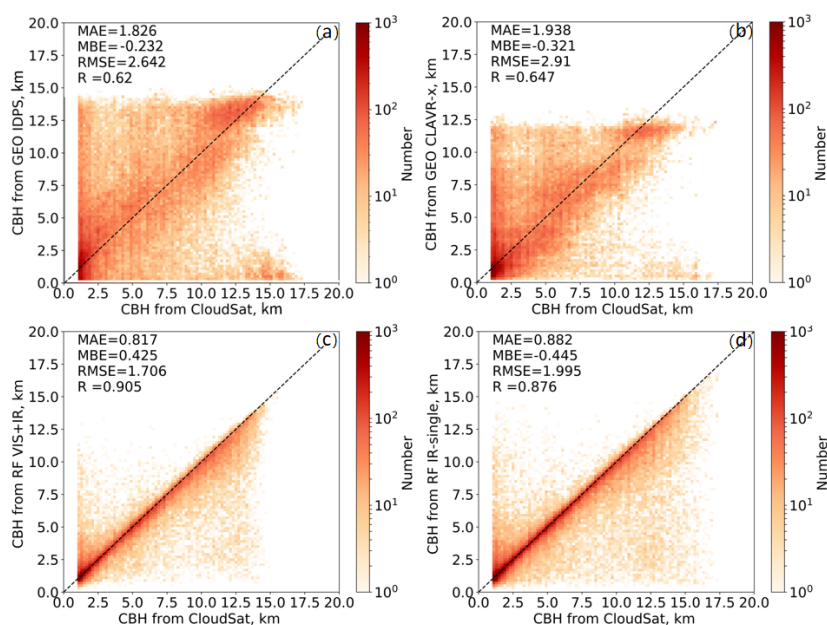
995

996

997



998



999

1000 **Figure 2.** Density distributions of CBHs retrieved from (a) GEO IDPS, (b) GEO  
1001 CLAVR-x, (c) VIS+IR and (d) IR-single algorithms compared with the CBHs from  
1002 the joint CloudSat/CALIPSO product (taken as true values) in 2017. The mean  
1003 absolute error (MAE), mean bias error (MBE), root mean square error (RMSE) and R  
1004 are listed in each subfigure where the difference exceeds the 95% significance level ( $p$   
1005  $< 0.05$ ) according to the Pearson's  $\chi^2$  test.

1006

1007

1008

1009

1010

1011

1012

1013

1014

1015

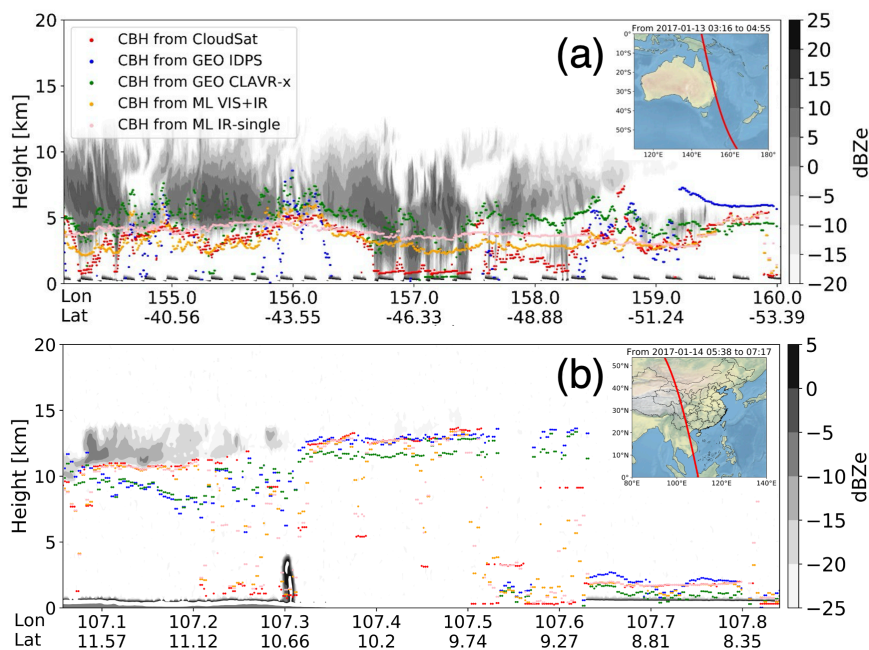
1016

1017





1018



1019

1020 **Figure 3.** Inter-comparisons of CBH products retrieved by CloudSat (red solid circle),  
1021 the GEO IDPS algorithm (blue solid circle), the GEO CLAVR-x (green solid circle),  
1022 the ML-based VIS+IR model algorithm (orange solid circle), and the ML-based  
1023 IR-single model algorithm (pink solid circle) at (a) 03:16–04:55 UTC on January 13,  
1024 2017 (a) and (b) 05:38–07:17 UTC on January 14, 2017. The black and gray colormap  
1025 represents the matched CloudSat radar reflectivity.

1026

1027

1028

1029

1030

1031

1032

1033

1034

1035

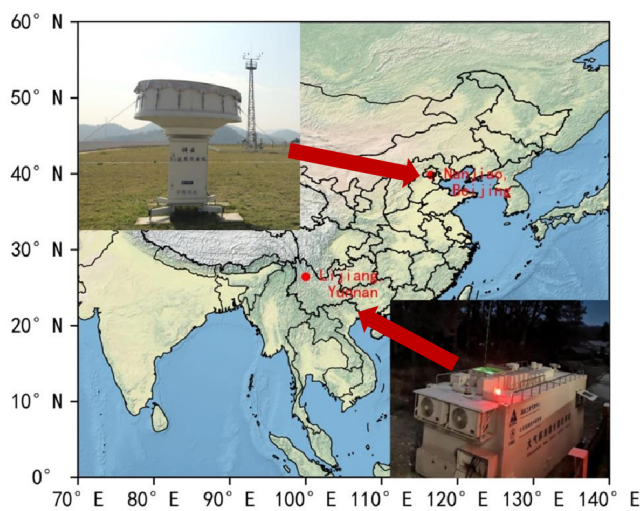
1036





1037

1038



1039

1040 **Figure 4.** Geographical locations and photos of lidar and cloud radar at Yunnan

1041 Lijiang and Beijing Nanjiao stations.

1042

1043

1044

1045

1046

1047

1048

1049

1050

1051

1052

1053

1054

1055

1056

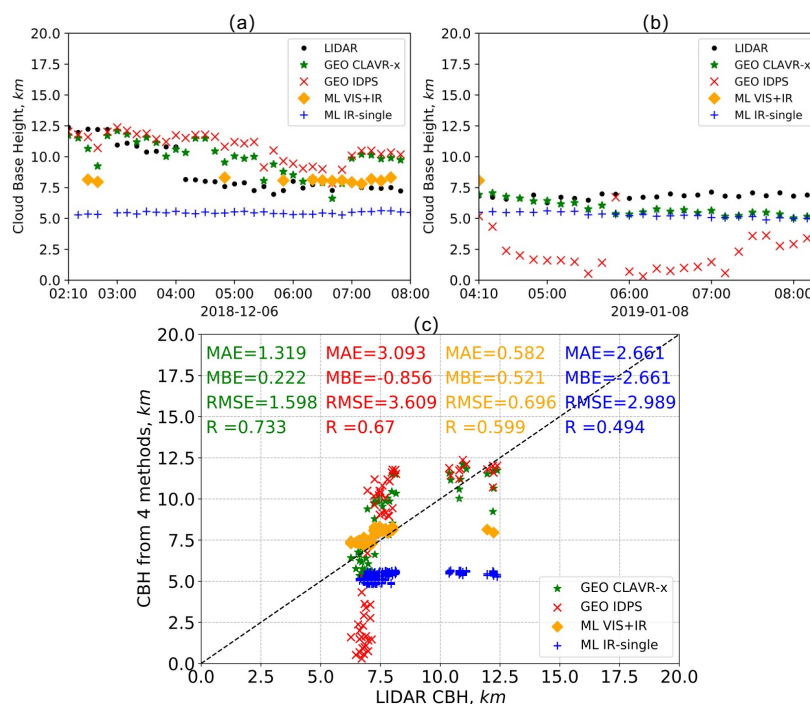
1057

1058

1059



1060



1061

1062 **Figure 5.** Comparisons of the CBHs from the ground-based lidar measurements  
 1063 (black solid circle) at Yunnan Lijiang station and the four GEO satellite retrieval  
 1064 algorithms, namely the GEO IDPS (red cross symbol), the GEO CLAVR-x (green  
 1065 solid asterisk), the ML-based VIS+IR model (orange solid diamond) and the  
 1066 ML-based IR-single model (blue plus sign) algorithms. Fig 6a and 6b show the time  
 1067 series of CBHs from lidar and the four GEO satellite retrieval algorithms on  
 1068 December 6, 2018 and January 8, 2019, respectively. Fig 6c shows the scatterplots of  
 1069 CBH samples from the lidar measurements and the four retrieval algorithms.

1070

1071

1072

1073

1074

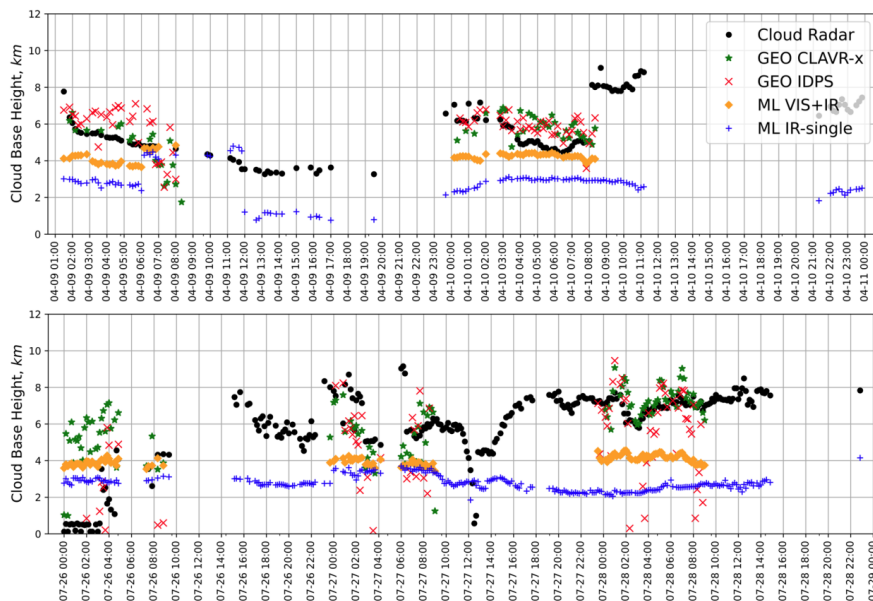
1075

1076



1077

1078



1079

1080 **Figure 6.** Same as Fig. 5, but for the CBH sample results from the cloud radar at  
1081 Beijing Nanjiao station (black solid circle) on April 9–10, 2017 (top panel) and July  
1082 26–28, 2017 (bottom panel).

1083

1084

1085

1086

1087

1088

1089

1090

1091

1092

1093

1094

1095

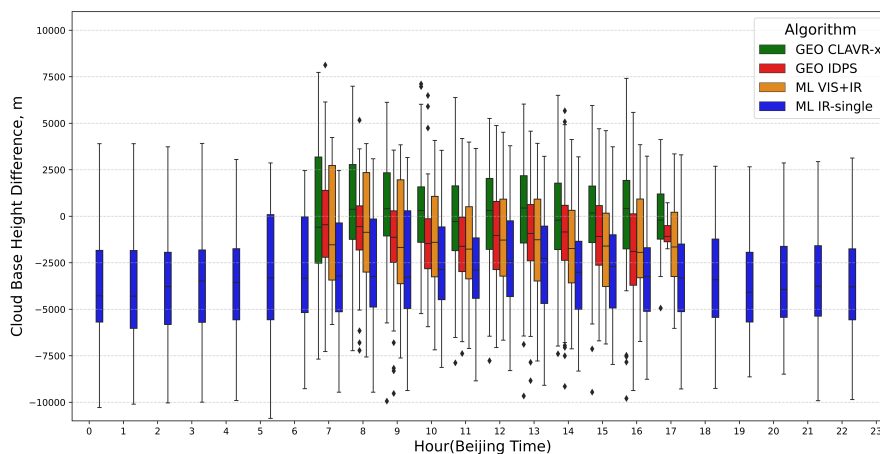
1096



1097

1098

1099



1100

1101 **Figure 7.** Box plots of the hourly CBH errors of four GEO satellite retrieval  
1102 algorithms (GEO IDPS, GEO CLAVR-x, ML-based VIS+IR and ML-based IR-single)  
1103 relative to the CBHs from the cloud radar at Beijing Nanjiao station in 2017. The box  
1104 symbols signify the 25th, 50th and 75th percentiles of errors. The most extreme  
1105 sample points between the 75th and outlier, and the 25th percentiles and outliers are  
1106 marked as whiskers and diamonds, respectively. Except for the period between 7 and  
1107 17 UTC (local time), the three algorithms of GEO CLAVR-x, GEO IDPS, and ML  
1108 VIS+IR are unavailable due to the lack of reflected solar radiance measurements.

1109

1110

1111

1112

1113

1114

1115

1116

1117

1118

1119

1120

1121

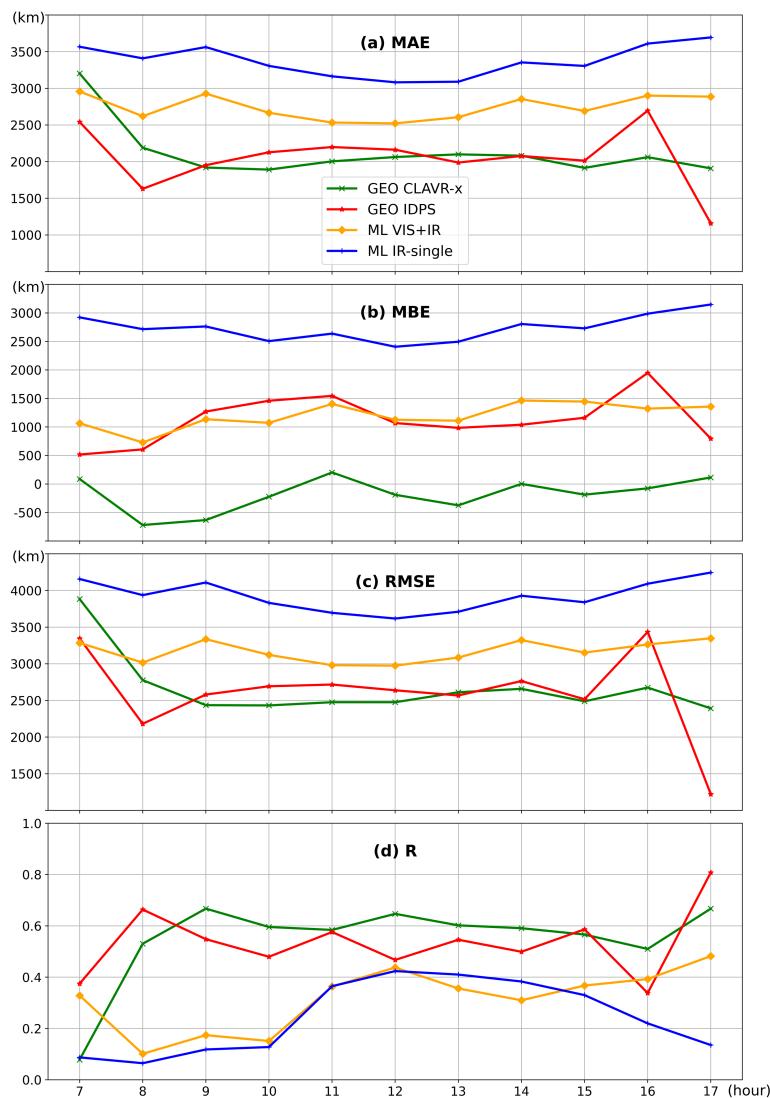
1122

1123

1124



1125



1126

1127 **Figure 8.** Comparisons of hourly (a) MAE, (b) MBE, (c) RMSE, and (d) R of CBH

1128 (relative to the CBHs from the cloud radar at Beijing Nanjiao station) from 07 to 17

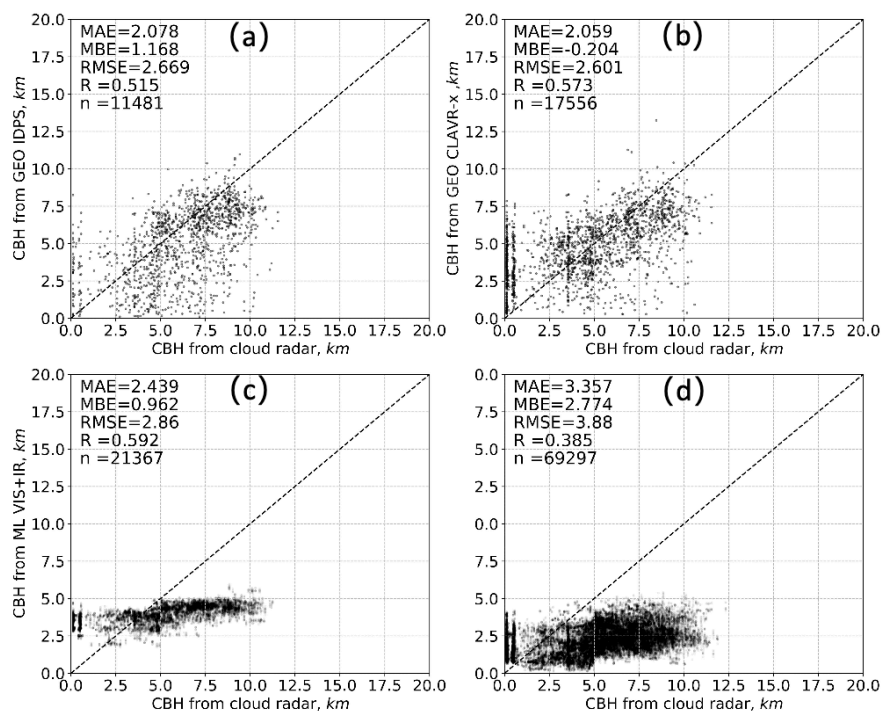
1129 (local time) between four retrieval algorithms (GEO IDPS, GEO CLAVR-x,

1130 ML-based VIS+IR and ML-based IR-single) in 2017.

1131

1132

1133



1134

1135 **Figure 9.** Comparisons between the CBHs from the cloud radar at Beijing Nanjiao  
1136 station and the matched CBHs from the four retrieval algorithms (GEO IDPS, GEO  
1137 CLAVR-x, ML-based VIS+IR and ML-based IR-single) in 2017.

1138

1139

1140

1141

1142

1143